Alexandria Engineering Journal 102 (2024) 159–168

Contents lists available at ScienceDirect

Alexandria Engineering Journal

journal homepage: www.elsevier.com/locate/aej

Original article

Optimised linear active disturbance rejection control of multiport-isolated DC-DC converter for hydrogen energy storage system integration

Oyedotun E. Oyewole [a,*], Ali A. Abdelaziz [a], Isah A. Jimoh [a], Eugene Bari [b], Khaled H. Ahmed [a]

[a] Department of Electronic and Electrical Engineering, University of Strathclyde, Glasgow G1 1XQ, UK
[b] Ecomar Propulsion Ltd., 32 Standard Way, Fareham PO16 8XG, UK

ARTICLE INFO

Keywords:
Decoupling
Hydrogen energy storage
Linear active disturbance rejection control
Linear extended state observer
Multiport-isolated DC-DC converter

ABSTRACT

Hydrogen energy storage systems are becoming increasingly accepted owing to their environmental friendliness. The efficiency and performance of these systems largely depend on the attributes of their power electronic interface systems. Among the promising solutions is a multiport-isolated DC-DC converter with characteristics of reduced component count, fewer conversion stages, and galvanic isolation. However, this system presents a challenge due to its inherent cross-coupling effect, complicating precise control. To address this, linear active disturbance rejection control (LADRC) is a viable option, leveraging dynamic/disturbance properties observed by linear extended state observers. LADRC serves as a decoupling controller, mitigating the cross-coupling effect. However, LADRC has several gains, and selecting them can be a difficult task, often requiring manual tuning. To streamline this process, this paper proposes utilising particle swarm optimisation to determine the optimum gains of LADRC. By employing this approach, the implementation of LADRC is facilitated with reduced design efforts while ensuring effective decoupling control within the system. Simulations are conducted to validate the performance of the optimised gain LADRC.

1. Introduction

Hydrogen Energy Storage System (HESS) is a versatile technological solution designed for energy storage, electricity generation, and various other applications in the power sector. Hydrogen is considered a promising sustainable alternative to conventional fossil fuels owing to its adverse environmental impacts. However, hydrogen does not occur naturally in isolation; it must be chemically extracted from compounds such as water. The central process of the HESS involves electrolysis through electrolysers (EL), where water undergoes separation into hydrogen and oxygen. Isolated hydrogen is then stored, and electricity is produced using fuel cells (FC). Various technologies for constructing EL and FC have been documented in the literature, including proton exchange membranes, alkaline and solid oxide technologies. HESS are environmentally friendly and have applications in transportation systems (e.g. hybrid electric vehicles), commercial/residential heating, and standalone electricity generation [1].

The standalone electricity generation concept, based on the three primary stages of HESS, hydrogen production, storage, and re-electrification [2] is depicted in Fig. 1. This can be described in two stages: (1) The surplus energy from the distributed energy source (DE) drives the EL to produce hydrogen, which is then stored in long-term hydrogen storage tanks. (2) During downtime, or when electricity from the DE is unavailable, the FC generates electricity through the stored hydrogen, as shown in Fig. 1.

To maintain the smooth operation of an HESS, specific features are required in its interfacing systems (power electronics converters), including high flexibility in the conversion ratio, minimal current ripple, high efficiency, and robust fault tolerance. Although numerous interfacing systems integrating fuel cells (FC) alone have been extensively documented in the literature, there has been relatively little discussion regarding interfacing systems for EL and the entire HESS [3]. Furthermore, achieving these specific features for a conventional HESS with one converter at every conversion stage [4] can be challenging. To address these limitations, multiport DC-DC converters have been developed, which offer a reduced number of independently operating converters. A multiport-isolated DC-DC converter, such as a triple active bridge (TAB), is easier to cascade and has fewer component counts [5,6]. The multiport-isolated DC-DC converter exhibits some advantages over its non-isolated counterparts, as illustrated in Table I, [7].

Multiport-isolated DC-DC converters function as multiple-input, multiple-output systems with interconnected power loops. Owing to the utilisation of multiwinding transformers in the converter, cross-

* Corresponding author.
E-mail address: oyedotun.oyewole@strath.ac.uk (O.E. Oyewole).

https://doi.org/10.1016/j.aej.2024.05.107
Received 13 February 2024; Received in revised form 28 May 2024; Accepted 28 May 2024
Available online 7 June 2024

Nomenclature

L_1, L_2', L_3' Leakage Inductances for DE, FC, and EL windings of the transformer
u_1, u_2', u_3' DE, FC, and EL bridge midpoint voltages
i_1, i_2', i_3' DE, FC, and EL bridge leakage inductor current
i_{2p}, i_{3p} Prefiltered output current at FC and EL ports respectively
$1 : n_2$ DE to FC turns' ratio
$1 : n_3$ DE to EL turns' ratio
V_{DE}, V_{FC}, V_{EL} Output voltages of the DE, FC, and EL ports respectively
P_{DE}, P_{FC}, P_{EL} Active output powers of the DE, FC, and EL ports respectively
I_{DE}, I_{FC}, I_{EL} Output current flowing towards or outside the DE, FC, and EL ports respectively
i_{12}, i_{23}, i_{13} Current flowing between the DE to FC bridge, the current flowing between the FC to EL bridge, and the current flowing between the DE to EL bridge respectively
P_{12}, P_{23}, P_{13} Power flowing between DE to FC bridge, power flowing between FC to EL bridge, and power flowing between DE to EL bridge respectively
φ_2 The phase shift between DE bridge and FC bridge voltages
φ_3 The phase shift between DE bridge and EL bridge voltages
L_{FC}, C_{FC} Inductance and capacitance of the LC filter at the FC port
r_{FC} Lumped FC port parasitic resistance
C_{EL} Capacitor filter at the EL port
f_{FC}, f_{EL} Lumped disturbance of both internal dynamics and external disturbance at FC and EL ports respectively
$\beta_1, \beta_2, \beta_3$ Observer gains
w_0 Observer bandwidths
K_p, K_d Controller gains
w_c Controller bandwidths
b_0 Critical gain
A_3, B_3, C_3, L_3 First-order state matrices
A_2, B_2, C_2, L_2 Second-order state matrices

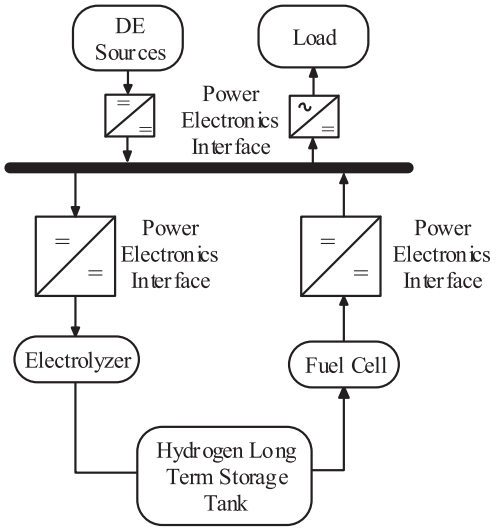

Fig. 1. Hydrogen energy storage system with a conventional power electronics interface.

Table I
Basic comparison between multiport-isolated and non-isolated converters.

	Isolated	Non-isolated
Galvanic isolation	Yes	No
Voltage matching	Can connect sources with different voltage levels	Sources are directly linked
Complexity	High	Moderate
Conversion stages	Less	More
Ease of cascade/ flexibility	High	Moderate
Control	Centralised control	Decentralised control
Power flow management	Simple and fast	Slow and complicated

coupling effects exist among its ports, which makes precise control challenging. This situation poses the risk of hydrogen depletion in the FC and unstable hydrogen production in the EL in the event of sudden system changes caused by cross-coupling. Consequently, fuel cells may consume more hydrogen than necessary, leading to suboptimal performance and energy wastage [8,9]. Therefore, effective decoupling control is needed to address these issues.

As discussed in [10–13] a decoupling controller was devised to mitigate cross-coupling effects by utilising a calculated system matrix. However, its implementation requires the computation and storage of the system matrix data for each feasible operating region, thereby increasing the complexity of the controller. An alternative approach was proposed in [14], wherein the system was configured to operate as a single-input, single-output system by adjusting the bandwidth. Specifically, the loop with the highest bandwidth was employed to ascertain the phase direction during transients, thereby facilitating decoupling control. Conversely, the loop with the lowest bandwidth exhibits inferior anti-interference properties. Another approach, as presented in [15] and [16], involves the development of a zero-source port leakage inductance multiport-isolated converter with a conventional PI controller. Although this design inherently possesses decoupling capabilities, its effectiveness in large systems remains unproven. In addition, an adaptive perturb and observe (P&O) controller outlined in [17] was introduced to track the minimum point current. However, the incorporation of the P&O algorithm increased the complexity of the controller. Generally, these decoupling controllers require a comprehensive understanding of the system parameters, which may fluctuate during operation. Furthermore, their implementation is challenging owing to complex computations or hardware constraints.

Therefore, there is a need to develop decoupling control methods that require minimal system parameter information and control complexity, while also considering the internal dynamic characteristics of the converter. Based on the existing literature, a linear active disturbance rejection controller (LADRC) is a promising solution that can estimate and reject both external and internal disturbances. It operates effectively with minimal system parameter information, typically requiring only the order of the plant and minimal computational requirements [18,19]. Consequently, it is suitable as an effective decoupling controller. The effectiveness of the LADRC has been demonstrated across various power electronic converter topologies, as seen in [20–22]. The applications range from T-type three-level converters to three-phase voltage source rectifiers and multilevel interleaved bidirectional DC-DC converters, showcasing LADRC's ability to achieve decoupling controls. The same principle was applied in [23,24] for the buck converter. Similarly, the controller was implemented in isolated converters. In [25], a LADRC decoupling control strategy was developed for an LLC resonant converter in an electric vehicle to enhance its dynamic performance and mitigate external and internal disturbances. In [26], a dual active bridge converter-based LADRC with a line expansion state observer was devised as a real-time decoupling

control to mitigate internal and external disturbances. Existing literature proposes various manual LADRC gains tuning methods [27–29], but these methods still require subjective determination of one or more parameters. In the context of a multiport-isolated DC-DC converter, a linear extended state observer (LESO)-based controller incorporating input matrix diagonalisation was developed for decoupling control in a quad-active bridge DC-DC converter [30,31], yielding a robust system with good decoupling control performance. In addition, LADRC with a high-bandwidth LESO was developed in [32] as a model-independent decentralised decoupling control. However, these applications, particularly for multiport-isolated DC-DC converters, do not clearly show the methods for selecting all controller gains, which can be more than just one or two. Selecting controller gains is crucial for decoupling control in multiport-isolated converters, ensuring appropriate control signals and system performance. However, current manual approaches are subjective, with significant design effort, and may not achieve optimal decoupling control.

A LADRC gain auto-tuning mechanism is essential for simplifying the decoupling control design. This paper proposes utilising particle swarm optimisation to determine the optimum gains of LADRC. The main contributions of this paper are as follows.

1. Introduction of an offline particle swarm optimisation approach to determine the optimal gains of the controller without imposing additional computational burden on the controller.
2. The identified optimal gains simplify the controller design process, bypassing the subjective nature of manual tuning methods.
3. Because the determined gains are the optimum gains for the controller, with the objective of reducing the observer's estimation error, satisfactory decoupling control performance can be ensured.

The optimised gain LADRC consists of a controller with a high-bandwidth LESO, and gain optimisation based on particle swarm optimisation (PSO).

The remainder of this paper is organised as follows. The multiport-isolated DC-DC converter and cross-coupling effects are discussed in Section II. Section III discusses the mathematical framework of the LADRC decoupling control for a TAB converter and Section IV discusses the optimisation technique and optimisation problem. The results obtained from the TAB converter are presented and discussed in Section V.

2. Multiport-isolated DC-DC converter

The three-port isolated DC-DC converter is presented in this section.

2.1. Topology analysis

The TAB is illustrated in Fig. 2. It is composed of three full bridges magnetically coupled by a three-winding transformer with a turn ratio of $1 : n_2 : n_3$.

For simplicity of analysis, DE and FC are represented as voltage sources in port 1 (DE port) and port 2 (FC port), respectively. The EL is represented as a resistive load at port 3 (EL port). L_1, L_2', and L_3' are the equivalent leakage inductances of the transformer at each port. The phase shift angles (φ_2 and φ_3) control the power flow between the ports while fixing the primary port at a zero phase shift.

To perform power flow analysis, it is crucial to determine the equivalent inductance between each port. This can be achieved by converting the star model into a delta model, as illustrated in Fig. 3. For convenience, all related circuit properties are referred to the primary side, as described in [11].

Using cycle-by-cycle averaging, the power transfer between any two ports in the delta model is expressed as seen in (1):

$$P_{ab} = \frac{\varphi(\pi - \varphi) V_a V_b}{2\pi^2 f_s L_{ab}} \tag{1}$$

where, a and b represent port numbers 1, 2, or 3; V_a and V_b are the

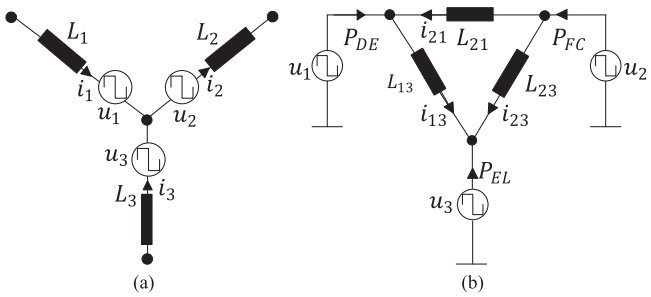

Fig. 3. Equivalent circuit of the converter: (a) Star model and (b) Delta model.

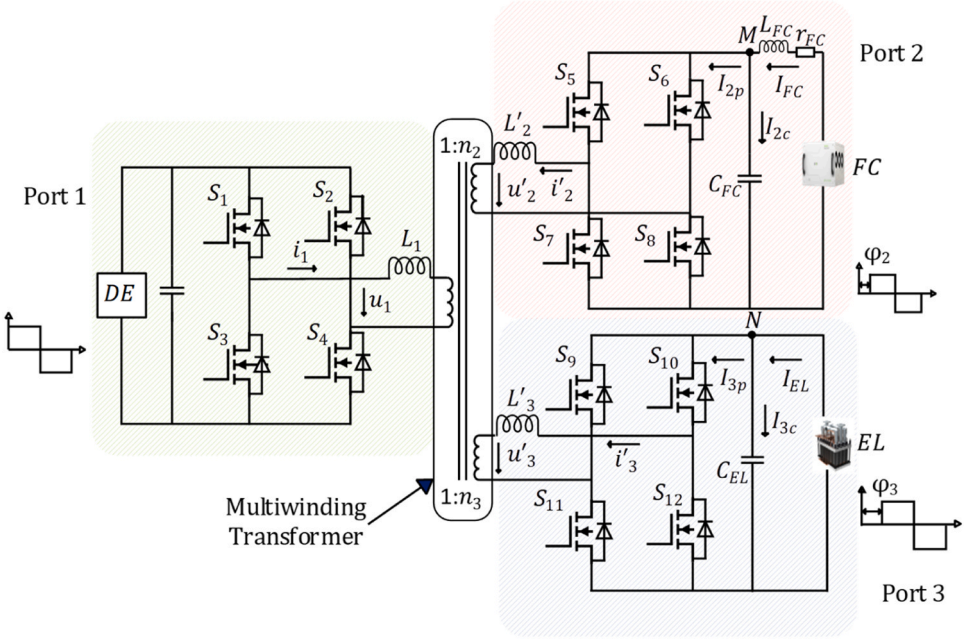

Fig. 2. Multiport-isolated DC-DC converter for hydrogen energy storage systems.

voltages of the two ports; f_s represents the switching frequency; φ is the phase difference (control inputs); and L_{ab} is the port inductance.

Similarly, the powers P_{DE}, P_{FC}, and P_{EL} which are the total output active powers in each port, are calculated, as shown in (2) – (4). The equations show a non-linear relationship between the output power and the control inputs.

$$P_{FC} = \frac{\varphi_2(\varphi_2 - \pi)V_{DE}V_{FC}L_3 + (\varphi_3 - \varphi_2)(\varphi_2 - \varphi_3 - \pi)V_{FC}V_{EL}L_1}{2\pi^2 f_s A} \tag{2}$$

$$P_{EL} = \frac{\varphi_3(\pi - \varphi_3)V_{DE}V_{EL}L_2 + (\varphi_3 - \varphi_2)(\pi - \varphi_2 + \varphi_3)V_{FC}V_{EL}L_1}{2\pi^2 f_s A} \tag{3}$$

$$P_{EL} + P_{FC} + P_{DE} = 0 \tag{4}$$

2.2. Cross-coupling Effects in TAB and Conventional Solution

To evaluate the controllability of a multiport-isolated DC-DC converter, a simplified model is required to demonstrate how the control inputs affect the output. The application of state-space generalised average modelling, which is typically utilised to analyse the dynamics of a DC-DC converter, faces challenges in the context of an isolated converter. This is because the equivalent leakage inductance currents serve as state variables and their integral value over one switching cycle is zero; hence, the dynamics of the leakage inductances are conventionally not considered.

From (2) – (4), the power flow exhibits a non-linear relationship. Hence, a small signal analysis of the system is required to linearise the system at an operating point closest to the origin [10,11]. The linearised system at an operating point is shown in (5).

$$\begin{bmatrix} I_{2p} \\ I_{3p} \end{bmatrix} = \begin{bmatrix} G_{11} & G_{12} \\ G_{21} & G_{22} \end{bmatrix} \begin{bmatrix} \varphi_2 \\ \varphi_3 \end{bmatrix} \tag{5}$$

where, I_{2p}, I_{3p} are pre-filtered currents and φ_2, φ_3 represent the phase shifts. The individual elements of the system matrix G can be expressed as:

$$\begin{aligned} G_{11} &= \frac{4(V_{EL}L_1 + V_{DE}L_3)}{\pi^3 f_s A} & G_{12} &= \frac{-4V_{EL}L_1}{\pi^3 f_s A} \\ G_{21} &= \frac{-4V_{FC}L_1}{\pi^3 f_s A} & G_{22} &= \frac{4(V_{FC}L_1 + V_{EL}L_2)}{\pi^3 f_s A} \end{aligned} \tag{6}$$

The non-diagonal elements in (6) are non-zero entities. Hence, the power flow controls between ports are cross-coupled. To minimise the cross-coupling effects, non-diagonal elements must be made to approach zero.

3. Decoupling control using LADRC

LADRC is a relatively new control algorithm designed as an alternative to the conventional proportional integral derivative (PID) control. It follows the basic idea of PID independence from a system's specific model but attempts to compensate for its weaknesses in terms of uncertainties, disturbance estimation, and subsequent rejection [19,32]. Cross-coupling effects are internal interactions/dynamics which can be treated as disturbances. Thus, LADRC can be implemented in multivariable decoupling controls [33]. While the foundational principles of LADRC have been documented in the literature [32–34], it is emphasised here to highlight the significance of its fundamental design gains essential for ensuring reliable control performance. Additionally, a mathematical representation of the gains tailored to the specific application of the TAB is derived.

3.1. Fundamental principles of LADRC

A conventional second-order plant expressed in the following form (7) is built up to the LADRC second-order control process in (8).

$$\ddot{y} = -a_1\dot{y} - a_2 y + d + bu \tag{7}$$

where, y is the system output, a_1 and a_2 are unknown constants, d is a disturbance, b is the critical gain, and u is the plant control input.

Eq. (7) can be further expressed as (8):

$$\ddot{y} = f(t, y, \dot{y}, d) + b_0 u \tag{8}$$

where, $f(t, y, \dot{y}, d) = -a_1\dot{y} - a_2 y + d + (b - b_0)u$ is an unknown lumped term which represents the total external disturbance and internal dynamics and b_0 is the nominal value of the critical gain which can be estimated from the nominal values of the energy storage elements of the system. If the lumped term value can be determined, it can be compensated for in real time. This is the basic concept of LADRC. Hence, a LESO can be used to observe both the state of the system and lumped term.

The states of the second-order plant are defined in (9):

$$x_1 = y \quad x_2 = \dot{y} \quad x_3 = f(t, y, \dot{y}, d) \tag{9}$$

where, x_3 denotes the extended state. Subsequently, (9) can be expressed into a matrix form (10),

$$\dot{x} = Ax + Bu + E\dot{f} \quad y = Cx \tag{10}$$

$$A = \begin{bmatrix} 0 & 1 & 0 \\ 0 & 0 & 1 \\ 0 & 0 & 0 \end{bmatrix}, B = \begin{bmatrix} 0 \\ b_0 \\ 0 \end{bmatrix}, C = \begin{bmatrix} 1 \\ 0 \\ 0 \end{bmatrix}^T, E = \begin{bmatrix} 0 \\ 0 \\ 1 \end{bmatrix},$$

and $\dot{f}$ represent the dynamics of the lumped term which is assumed to be bounded. Designing an extended observer for the system yields (11).

$$\dot{z} = Az + Bu + L\widehat{e y} = Cz \tag{11}$$

where, L is a matrix containing β_1, β_2, and β_3 which are the observer gains, $e = (y - \hat{y})$ is the error between the estimated output and system output (observer's estimation error), and z is the observer estimate. The observer gains are chosen as a function of the observer bandwidth, using bandwidth parameterisation [34], as shown in (12):

$$\beta_1 = 3w_0 \quad \beta_2 = 3w_0^2 \quad \beta_3 = w_0^3 \tag{12}$$

A well-tuned observer can track y, $\dot{y}$ and $\dot{f}$ through z_1, z_2, and z_3. Subsequently, the LADRC can compensate for the cross-coupling effects by eliminating the third state z_3, which can be obtained by (13):

$$u = \frac{u_0 - z_3}{b_0} \tag{13}$$

Applying (13) to (8) yields the following relation (14):

$$\ddot{y} = u_0 \tag{14}$$

This can be easily achieved using a simple proportional derivative controller, as shown in (15).

$$u_0 = k_p(ref - z_1) - k_d z_2 \tag{15}$$

where, u_0 denotes the system control input. The controller gains k_p and k_d can be derived from the controller bandwidth [34], as in (16).

$$k_p = w_c^2 \; k_d = 2w_c \tag{16}$$

The introduction of bandwidth parameterisation [34] notably reduces the number of LADRC gains that require tuning. This leaves three crucial gains to be tuned for second-order LADRC, as illustrated by the dotted lines in Fig. 4. This scenario is analogous to a first-order plant except for $\dot{y}$ in the lumped term [33,35]. The critical gain b_0 dictates the controller's sensitivity to disturbances, with higher values indicating greater sensitivity. Observer gains determined by the observer bandwidth w_0 influence the disturbance estimation of the system. Higher values lead to faster disturbance estimation and error tracking. The

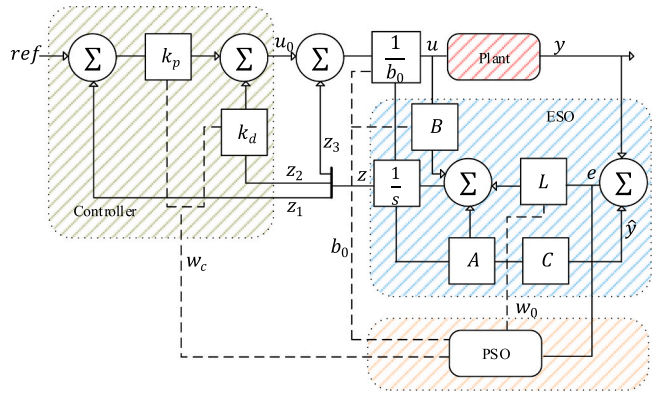

Fig. 4. Typical LADRC schematic for second-order plant. (The controller is shown in the green shaded box, the LESO in the blue shaded box, PSO in the orange shaded box while the dashed lines represent the PSO outputs used to determine the critical gain, controller gains and observer gains).

controller gains, derived from the controller bandwidth w_c, dictate the intensity of control actions in response to estimated disturbances and tracking errors. Extreme values, whether too high or too low, tend to result in noisy, oscillating, or inadequate tracking signals.

3.2. Lumped term and gains expression for TAB

The system consists of two control loops: the current control loop at the FC port with an LC filter is analysed as a second-order plant, and the voltage control loop at the EL port is modelled as a first-order plant. Kirchoff's voltage and current laws are applied at node M as shown in Fig. 2. Considering the dynamics of the LC filter and combining it with (5) yields the second-order equation in (17):

$$I''_{FC} = \frac{-I_{FC}}{L_{FC}C_{FC}} - \frac{r_{FC}}{L_{FC}} I'_{FC} + \frac{G_{11}\varphi_2}{L_{FC}C_{FC}} + \frac{G_{12}\varphi_3}{L_{FC}C_{FC}} \tag{17}$$

Writing (17) in the form of (8) yields (18),

$$I''_{FC} = f_{FC}\left(t, I_{FC}, I'_{FC}, d\right) + b_{0,FC}\varphi_2 \tag{18}$$

where,

$$f_{FC}\left(t, I_{FC}, I'_{FC}, d\right) = \frac{-I_{FC}}{L_{FC}C_{FC}} - \frac{r_{FC}}{L_{FC}} I'_{FC} + \frac{G_{12}\varphi_3}{L_{FC}C_{FC}} + \left(\frac{G_{11}}{L_{FC}C_{FC}} - \frac{G_{11,0}}{L_{FC,0}C_{FC,0}}\right)\varphi_2 \tag{19}$$

$$b_{0,FC} = \frac{G_{11,0}}{L_{FC,0}C_{FC,0}} \tag{20}$$

where, f_{FC} in (19) represents the lumped term, $b_{0,FC}$ in (20) is the critical gain, r_{FC} is the lumped parasitic resistance of the LC filter, and $G_{11,0}$, $L_{FC,0}, C_{FC,0}$ are the nominal values of G_{11}, L_{FC} , and C_{FC} respectively.

To observe f_{FC}, a LESO is designed based on (11) – (13), as given in (21) and (22)

$$\dot{z}_{FC} = [A_2 - L_2C_2]z_{FC} + [B_2 \quad L_2]u_2 \tag{21}$$

$$y_2 = z_{FC} \tag{22}$$

where, z_{FC} is the output of the observer tracking I_{FC}, I'_{FC}, and f_{FC}. The state-space matrices A_2, B_2, C_2, and L_2 follow the expression given in (10) and an input vector u_2 is $[\varphi_2 \quad I_{FC}]^T$.

Following the same principle, applying Kirchoff's voltage and current laws at node N yields the following first-order equation:

$$V'_{EL} = \frac{V_{EL}}{C_{EL}} + \frac{G_{21}\varphi_2}{C_{EL}} + \frac{G_{22}\varphi_3}{C_{EL}} \tag{23}$$

Writing (23) in the form of (8), gives (24)

$$V'_{EL} = f_{FC}(t, V_{EL}, d) - b_{0,EL}\varphi_3 \tag{24}$$

where,

$$f_{EL}(t, V_{EL}, d) = \frac{V_{EL}}{C_{EL}} + \frac{G_{21}\varphi_2}{C_{EL}} + \left(\frac{G_{22}}{C_{EL}} - \frac{G_{22,0}}{C_{EL,0}}\right)\varphi_3 \tag{25}$$

$$b_{0,EL} = \frac{G_{22,0}}{C_{EL,0}} \tag{26}$$

where, f_{EL} in (25) represents the lumped term, $b_{0,EL}$ in (26) is the critical gain, and $G_{22,0}, C_{EL,0}$ are nominal values of G_{22} and C_{EL}.

To observe f_{EL}, a LESO is designed based on (11) – (13), to derive (27) and (28)

$$\dot{z}_{EL} = [A_3 - L_3C_3]z_{EL} + [B_3 \quad L_3]u_3 \tag{27}$$

$$y_3 = z_{EL} \tag{28}$$

where, z_{EL} is the output of the observer tracking V_{EL} and f_{EL}. The state-space matrices A_3, B_3, C_3, and L_3 follow the expression given in (10), modified for a first-order plant, and the input vector u_3 is $[\varphi_3 \quad V_{EL}]^T$.

Similarly, in a stable open-loop system, for each loop $w_{0,EL}$ and $w_{0,FC}$ can be derived from the open-loop order response approximation. For second and first-order plants (29),

$$w_{0,FC} = \frac{5Q_{FC}}{t}, \; w_{0,EL} = \frac{8Q_{EL}}{t} \tag{29}$$

where, t is the settling duration and $Q_{FC} \geq 1$ and $Q_{EL} \geq 1$.

The controller bandwidths are related to the observer bandwidths as (30),

$$w_{c,FC} = \frac{w_{o,FC}}{Q_{FC}}, \; w_{c,EL} = \frac{w_{o,EL}}{Q_{EL}} \tag{30}$$

4. LADRC gain optimisation

Three gains are necessary for the LADRC design, as shown in Fig. 4. Conventionally, these gains are manually tuned which could be subjective. Consequently, there is a need for a more systematic approach to determine the optimal gains of LADRC. Utilising the potential estimation error within the observer, mathematically depicted in (11), as an input for determining the optimum gains promises to enhance the performance of the controller. The optimisation problem formulation and technique are discussed based on the aforementioned models, respectively.

4.1. Optimisation problem formulation

For a TAB-based LADRC, the objective is to minimise the observer's estimation error. This error represents the disparity between the estimated output and system output for both first- and second-order plants.

The state matrices, controller, and observer gains, for a second-order and first-order plant, following (10), (12), (16), and (30), respectively, are given as (31) – (34):

$$L_2 = \begin{bmatrix} 3w_{0,FC} \\ 3w_{0,FC}{}^3 \\ w_{0,FC}{}^2 \end{bmatrix} \quad B_2 = \begin{bmatrix} 0 \\ b_{0,FC} \\ 0 \end{bmatrix} \quad w_{c,FC} = \frac{w_{0,FC}}{Q_{FC}} \tag{31}$$

$$A_2 = \begin{bmatrix} 0 & 1 & 0 \\ 0 & 0 & 1 \\ 0 & 0 & 0 \end{bmatrix} \quad C_2 = [1 \quad 0 \quad 0] \tag{32}$$

$$L_3 = \begin{bmatrix} 2w_{0,EL} \\ w_{0,EL}{}^2 \end{bmatrix} \quad B_3 = \begin{bmatrix} b_{0,EL} \\ 0 \end{bmatrix} \quad w_{c,EL} = \frac{w_{0,EL}}{Q_{EL}} \tag{33}$$

$$A_3 = \begin{bmatrix} 0 & 1 \\ 0 & 0 \end{bmatrix} \qquad C_3 = [1 \quad 0] \tag{34}$$

where all terms are previously defined. Consequently, the estimated current and voltage is calculated as in (35) − (38)

$$I_{e,FC} = C_2(A_2 z_{FC} + B_2 \varphi_2) + L_2\left(I_{ei,FC} - I_{i,FC}\right) \tag{35}$$

$$e_{FC} = I_{e,FC} - I_{FC} \tag{36}$$

$$V_{e,EL} = C_3(A_3 z_{EL} + B_3 \varphi_3) + L_3\left(V_{ei,EL} - V_{i,EL}\right) \tag{37}$$

$$e_{EL} = V_{e,EL} - V_{EL} \tag{38}$$

where, $I_{i,FC}$ and $I_{ei,FC}$ are the initial current output and initial estimated current, respectively; I_{FC}, and $I_{e,FC}$ are the current output and estimated current of the second-order plant, respectively. Furthermore, $V_{i,EL}$ and $V_{ei,EL}$ are the initial voltage output and initial estimated voltage, respectively, while V_{EL} and $V_{e,EL}$ are the voltage output and estimated voltage of the first-order plant, respectively. The errors generated in the FC and EL ports are denoted as e_{FC} and e_{EL}, respectively.

The square mean error is implemented as the objective function as follows in (39):

$$J_{FC} = \underset{q,FC}{Min}\left(\frac{1}{n}\sum e_{FC}^2\right),\ J_{EL} = \underset{q,EL}{Min}\left(\frac{1}{n}\sum e_{EL}^2\right) \tag{39}$$

where, $q_{,EL} = \begin{bmatrix} w_{0,EL} \\ b_{0,EL} \end{bmatrix}$ and $q_{,FC} = \begin{bmatrix} w_{0,FC} \\ b_{0,FC} \end{bmatrix}$ are the optimisation variables, and n denotes the number of data points or samples.

4.2. Optimisation algorithm

The choice of the optimisation method is not fixed, provided it can handle non-linear problems. Nevertheless, PSO is chosen for its simplicity in implementation and versatility. Its effective memory capability allows potential solutions to recall past best solutions and compare them with neighbouring best solutions, fostering the generation of even better solutions. In essence, PSO efficiently performs global searches. In this paper, an alternative algorithm, the genetic algorithm (GA), is employed to benchmark the PSO. The GA implementation is based on standard binary coding and stochastic universal sampling as typified in [36]. Both algorithms are population-based search techniques that rely on information sharing among populations to improve their search processes through a blend of deterministic and probabilistic rules. Both can be applied to a wide range of optimisation problems without the need for problem specific knowledge. However, they differ in search strategies and mechanisms. Table II presents a summary of the comparisons between the two algorithms [37,38].

PSO imitates the swarm behaviour. Each particle in the sample space represents a potential solution to the optimisation problem. The initial velocity V and position X of each particle within the defined ranges of the decision variables are calculated using the basic equations given in [39], as shown in (40).

$$V_j^{n+1} = \omega V_j^n + c_1 r_1\left(Pbest_j^n - X_j^n\right) + c_2 r_2\left(Gbest^n - X_j^n\right) X_j^{n+1} = X_j^n + V_j^{n+1} \tag{40}$$

Table II
Comparison between PSO and GA.

	PSO	GA
Computational Efficiency	Higher	Lower
Ease of Implementation	Easier	Easy
Convergence Speed	Faster	Slower
Iteration	Fewer	More

where, n is the iteration index, c_1 and c_2 are constants set to 1.4962. Additionally, r_1 and r_2 are two randomly generated numbers between 0 and 1 and ω, inertia constant, taken as 0.7298. This yields Gbest (global best position) and Pbest (personal best position). The fitness of each particle at the initial position is evaluated iteratively using the optimisation objective. An update of each particle's position and velocity is then evaluated based on the initial best known position and global best known positions. The process is repeated until a position that fits the control objective is derived or the maximum number of iterations is reached.

The PSO algorithm follows the flow chart depicted in Fig. 5, and MATLAB software was used for offline gain calculations. Initially, a vector representing particle positions X (comprising the critical gain, observer bandwidths, and controller bandwidths) is generated randomly. The following steps are executed in each iteration:

1. At iteration n, each particle X_j^n is evaluated. This evaluation yields estimated current and voltage (evaluated at X_j^n) along with the objective function J_{FC} or J_{EL} (depending on the system's order)
2. The evaluation of the objective function J_{FC} or J_{EL} (evaluated at X_j^n) for each individual X_j^n is compared with its evaluation in the previous iteration. Thus, the particle position X_j^n that achieves the minimum best value is defined as $Pbest_j^n$.
3. This comparison in step 2 is made with respect to Eqs. (35) or (36) depending on the order of the system.
4. The Pbest that achieves the minimum e_{FC}^2 or e_{EL}^2 value within the entire swarm is defined as Gbest.
5. Utilising the basic equations of PSO (40), the velocity and position of the individuals are updated accordingly.
6. Upon completion of all iterations, gbest is identified, comprising the optimal bandwidths with minimum e_{FC}^2 or e_{EL}^2.

Finally, according to the formulations provided, the optimised gain

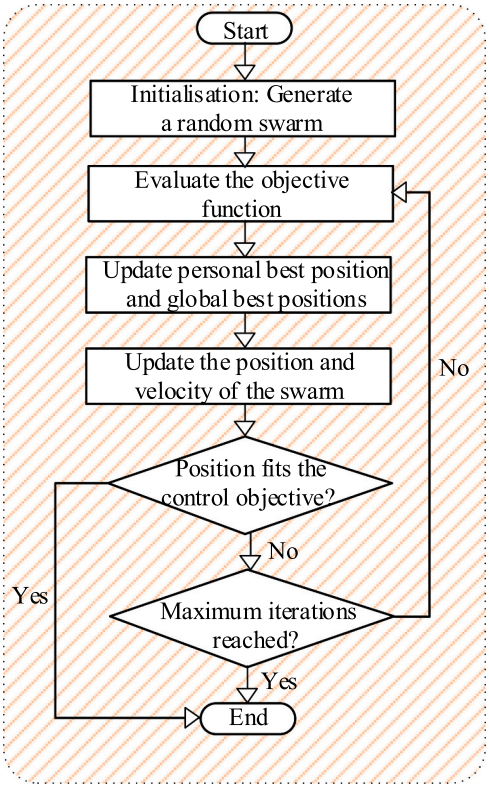

Fig. 5. PSO flow chart.

LADRC decoupling control with PSO schematics is depicted in Fig. 6.

The system control inputs are implemented as (41) and (42):

$$u_{FC} = k_p\left(I_{FC,ref} - I_{FC}\right) - k_d I'_{FC} \tag{41}$$

$$u_{EL} = k_p\left(V_{EL,ref} - V_{EL}\right) \tag{42}$$

while the actual plant control inputs are depicted in (43) and (44):

$$\varphi_2 = \frac{u_{FC} - f_{FC}}{b_{0,FC}} \tag{43}$$

$$\varphi_3 = \frac{u_{EL} - f_{EL}}{b_{0,EL}} \tag{44}$$

The actual plant control inputs φ_2 and φ_3 can deliver a decoupled control while ensuring adequate set point tracking.

5. Simulation results

Simulations are performed to substantiate the effectiveness of the optimised gain LADRC. The circuit is modelled using the SIMULINK/MATLAB simulation package, as illustrated in Fig. 2. The control schematic is implemented as shown in Fig. 6. Table III: lists the electrical specifications of the TAB DC-DC converter.

Two scenarios covering the worst-case conditions are considered in the simulations to validate the performance of the optimised gain LADRC. In the first scenario, the reaction of the corresponding ports is observed when the power supplied by the FC is varied. Hence, step changes are applied to P_{FC} at 0.05 s, 0.1 s and 0.15 s with −200 W to −1000 W, −1000 W to – 600 W and −600 W to −750 W respectively. During this process, the power absorbed by the EL port is maintained at 1000 W and the DE port acts as the slack port. The results of this scenario are shown in Fig. 7a. In the second scenario, the FC port maintains a constant power supply of 1000 W, while step changes are made to the power absorbed by the EL port within the same time intervals as in scenario 1, with variations from no power to 1000 W, 1000 W to 350 W, and 350 W to 100 W. The DE port serves as a slack bus, and the results are shown in Fig. 7b.

Cross-coupling effects are the internal interactions which manifest as disturbances. This can be quantified as the percentage of the power deviation (undershoot or overshoot) relative to the nominal value in response to intentional or unintentional modifications in the power supplied or absorbed by other ports. The lower this value, the better the decoupling control. The LADRC is designed to eliminate the lumped term, which is a combination of internal dynamics and external disturbances, to compensate for the cross-coupling effect. In this paper, the optimum gains of the LADRC are determined using PSO.

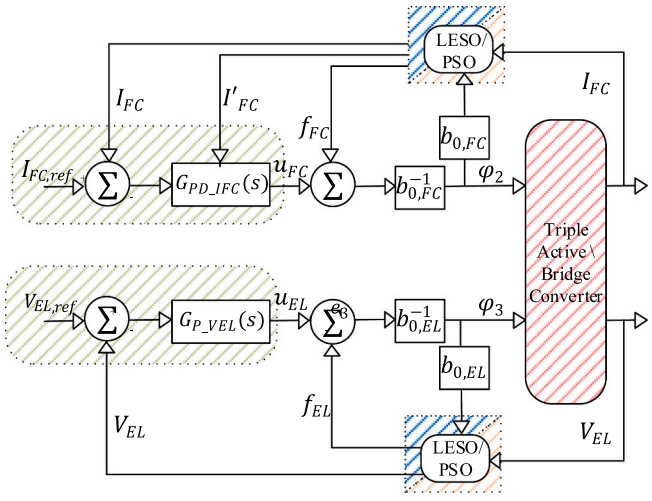

Fig. 6. Optimised gain LADRC decoupling control with PSO schematic.

Table III
TAB Converter and controller specifications.

Description	Symbol	Unit	Ports		
			#1	#2	#3
Voltage Rating	V_{DE}, V_{FC}, V_{EL}	V	560	46	73
Leakage Inductance	L_1, L'_2, L'_3	μH	780	4.992	13.18
Switching frequency	f_s	kHz	15	15	15
Transformer Turns Ratio	n_2, n_3	-	1	0.08	0.13
Optimised gain LADRC with PSO	w_0	rad/s	-	6.20e3	7.81e3
	w_c	rad/s	-	3.10e3	1.56e3
	b_0	-	-	6.94e7	4.71e3
	w_0	rad/s	-	7.51e3	5.82e3
Optimised gain LADRC with GA	w_c	rad/s	-	1.87e3	1.16e3
	b_0	-	-	5.26e7	5.42e3
PI controller	K_i	-	-	6000	8000
	K_p	-	-	15	10

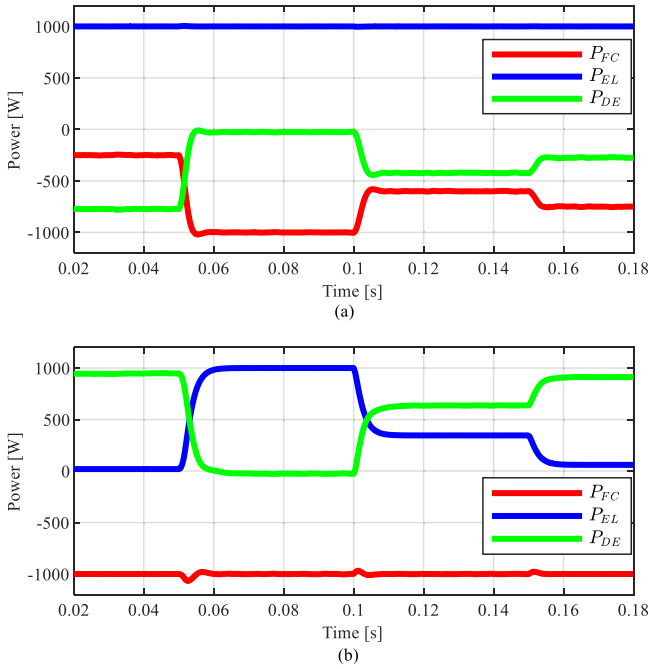

Fig. 7. Power transfer between ports using the optimised gain LADRC decoupling control with PSO: (a) Power absorbed by the EL when step changes are applied to the power supplied by the FC and E ports and (b) Power supplied by the FC port when step changes are applied to the power absorbed by the EL and DE ports.

First, the performance of the optimised gain LADRC with PSO is evaluated, as shown in Fig. 7. In the first scenario, the optimised gain LADRC with PSO exhibits a negligible power undershoot or overshoot from the nominal value at the EL port, as shown in Fig. 7a. While there are deviations in scenario 2, as depicted in Fig. 7b, these deviations are maintained at a minimum power undershoot and overshoot at the three applied step changes. Furthermore, a good power flow response is observed at the corresponding ports in each scenario.

In addition, simulations are carried out with optimised gain LADRC with GA and PI without decoupling control, as shown in Fig. 8 and Fig. 9 to ascertain the superiority of the optimised gain LADRC with PSO. For adequate comparison, the simulation utilises the average gains obtained from an equal number of runs of each optimisation method, as seen in

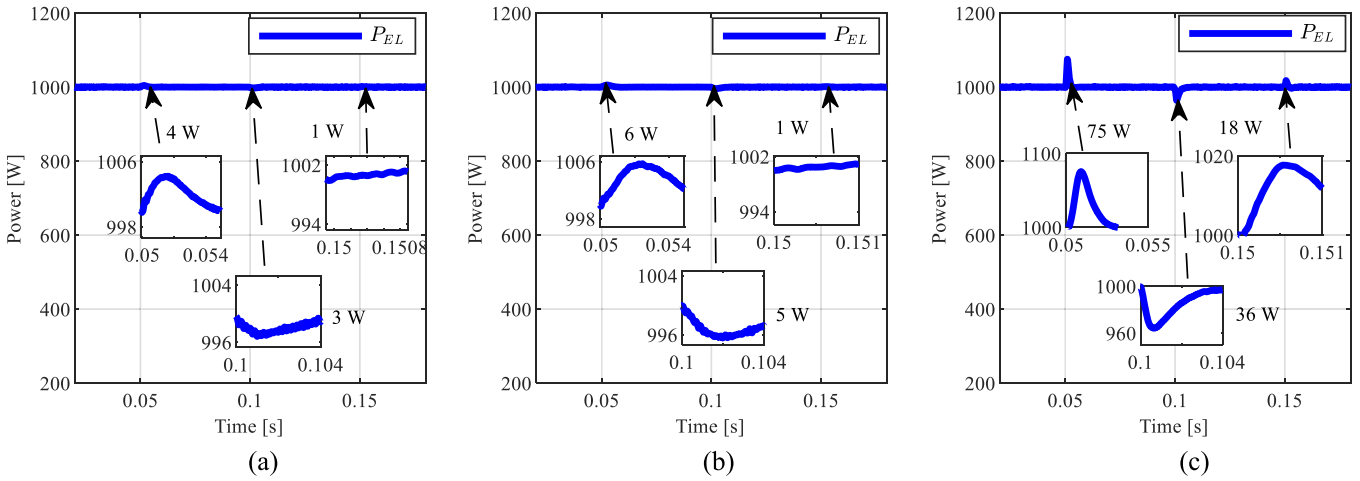

Fig. 8. The power absorbed by the EL when step changes are applied to the power supplied by the FC and DE ports for (a) Optimised gain LADRC decoupling control with PSO, (b) Optimised gain LADRC decoupling control with GA, and (c) PI without decoupling control.

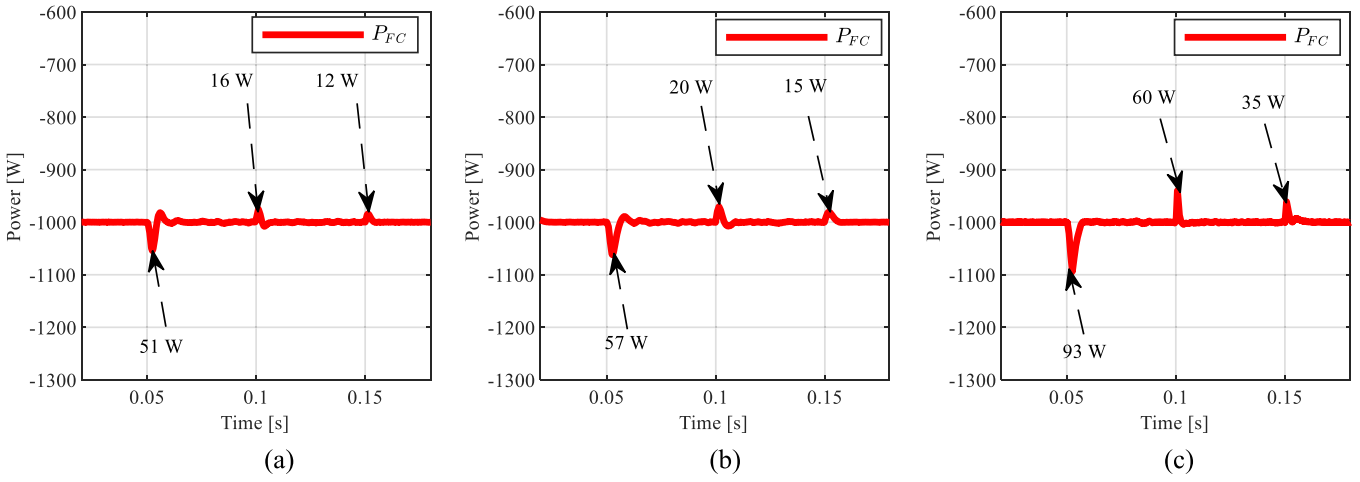

Fig. 9. Power supplied by the FC port when step changes are applied to the power absorbed in the EL and DE ports for (a) Optimised gain LADRC decoupling control with PSO, (b) Optimised gain LADRC decoupling control with GA, and (c) PI without decoupling control.

Table III. In scenario 1, the PI without decoupling control exhibits an 8 % overshoot, a 4 % undershoot, and a 2 % overshoot, as illustrated in Fig. 8c. On the other hand, the optimised gain LADRC with GA demonstrates a similar outcome of negligible power deviation with the optimised gain LADRC with PSO, as illustrated in Fig. 8a and Fig. 8b, respectively. This shows that the choice of the optimisation algorithm is not fixed if the optimisation objective is met.

Similarly, in scenario 2, The PI without decoupling exhibits 9 % undershoot, 6 % overshoot, and 4 % overshoot, as illustrated in Fig. 9c. On the other hand, the optimised gain LADRC with GA displays 6 % undershoot, 2 % overshoot, and negligible overshoot at the third step change, as depicted in Fig. 9b. In contrast, the optimised gain LADRC with PSO shows a 5 % undershoot, 2 % overshoot, and negligible power deviation at the third step change in this scenario, as observed in Fig. 9a. In this scenario, very similar results in the optimised gain LADRC with GA and the optimised gain LADRC with PSO can also be observed. However, a slightly improved result can be seen in the optimised gain LADRC with PSO, because of the specific characteristics of PSO. The summary of the results is shown in Table IV, a significant decoupling performance improvement can be seen with optimised gain LADRC with

Table IV
Summary of results.

Method	Step time (s)	Scenario 1			Scenario 2		
		Power deviation (W)	% deviation	% improvement	Power deviation (W)	% deviation	% improvement
PI without decoupling control	0.05	75	8	-	93	9	-
	0.1	36	4	-	60	6	-
	0.15	18	2	-	35	4	-
Optimised gain LADRC with PSO.	0.05	4	~ 0	71	51	5	42
	0.1	3	~ 0	33	16	2	44
	0.15	1	~ 0	17	12	~ 0	23
Optimised gain LADRC with GA	0.05	6	~ 0	69	57	6	36
	0.1	5	~ 0	31	20	2	40
	0.15	1	~ 0	17	15	2	20

PSO and GA as compared to the PI without decoupling control.

6. Conclusion

A multiport-isolated DC-DC converter possesses an inherent cross-coupling effect between its ports owing to the multiwinding transformer which makes precise control difficult. In this paper, the optimum gains of the LADRC are determined using PSO instead of manual tuning methods. The optimised gain LADRC with PSO is composed of a controller with high bandwidth LESO and PSO-based gain optimisation. The optimised gain LADRC with PSO is composed of a controller with high bandwidth LESO and PSO-based gain optimisation. The optimised gain LADRC provides an auto-tuning gain solution by generating an optimised gain through PSO, thus reducing the manual tuning complexities. First, the converter's control output relationship was established, and the cross-coupling effect was analysed. Furthermore, the mathematical expressions for LADRC were derived with PSO performing the optimisation in each control loop. The optimised gain LADRC with PSO satisfactorily suppresses the cross-coupling effect with the lowest power undershoot of 5 % compared to the power undershoots of 6 % and 9 % observed with the optimised gain LADRC with GA and PI without decoupling control methods across the two simulation scenarios considered. The LADRC gains were optimised, resulting in reduced design effort, and ensuring satisfactory decoupling control, as depicted in the results generated. Nevertheless, the controller was implemented using two control inputs, which are the two phase shifts. Future research may explore the possibility of incorporating an additional control input to improve the performance of the controller.

CRediT authorship contribution statement

Oyedotun E. Oyewole: Writing – review & editing, Writing – original draft, Validation, Methodology, Investigation, Conceptualization. **Khaled H. Ahmed:** Writing – review & editing, Supervision. **Eugene Barry:** Resources. **Ali A. Abdelaziz:** Writing – review & editing, Supervision. **Isah A. Jimoh:** Writing – review & editing.

Declaration of Competing Interest

The authors declare that they have no known competing financial interests or personal relationships that could have appeared to influence the work reported in this paper.

Acknowledgement

The authors wish to express their sincere appreciation to the Petroleum Technology Development Fund (PTDF) in West Africa, Nigeria for their generous sponsorship.

References

[1] E. Zoulias, E. Varkaraki, N. Lymberopoulos, C.N. Christodoulou, G.N. Karagiorgis, A review on water electrolysis, Tcjst vol. 4 (2) (2004) 41–71.
[2] P. Breeze, Chapter 8 - hydrogen energy storage, in: P. Breeze (Ed.), Power System Energy Storage Technologies, Academic Press, 2018, pp. 69–77.
[3] D. Guilbert, S.M. Collura, A. Scipioni, DC/DC converter topologies for electrolyzers: State-of-the-art and remaining key issues, Int. J. Hydrog. Energy vol. 42 (38) (2017) 23966–23985, https://doi.org/10.1016/j.ijhydene.2017.07.174.
[4] J. Li, Q. Luo, T. Luo, D. Mou, M. Liserre, Efficiency optimization scheme for isolated triple active bridge DC-DC converter with full soft-switching and minimized RMS current, IEEE Trans. Power Electron. vol. 37 (8) (2022) 9114–9128, https://doi.org/10.1109/tpel.2022.3157443.
[5] M. İnci, Ö. Türksoy, Review of fuel cells to grid interface: configurations, technical challenges and trends, J. Clean. Prod. vol. 213 (2019) 1353–1370, https://doi.org/10.1016/j.jclepro.2018.12.281.
[6] D. Vinnikov, A. Andrijanovitš, I. Roasto, T. Jalakas, Experimental study of new integrated DC/DC converter for hydrogen-based energy storage, 2011 10th Int. Conf. Environ. Electr. Eng. (2011) 1–4, https://doi.org/10.1109/EEEIC.2011.5874667.
[7] H. Tao, A. Kotsopoulos, J. Duarte, M. Hendrix, Family of multiport bidirectional DC-DC converters, Electr. Power Appl., IEE Proc. vol. 153 (2006) 451–458, https://doi.org/10.1049/ip-epa:20050362.
[8] D.M. Wu, C. Peng, C. Yin, H. Tang, Review of system integration and control of proton exchange membrane fuel cells, Electrochem. Energy Rev. (2020) 1–40.
[9] H. Dai, W. Tang, Modeling and simulation in fuel cells, in: R. Gupta (Ed.), Handbook of Energy Materials, Springer Nature Singapore, Singapore, 2022, pp. 1–45.
[10] K. Nishimoto, Y. Kado, K. Wada, Implementation of decoupling power flow control system in triple active bridge converter rated at 400V, 10kW, and 20kHz, IEEJ J. Ind. Appl. vol. 7 (5) (2018) 410–415, https://doi.org/10.1541/ieejjia.7.410.
[11] C. Zhao, S.D. Round, J.W. Kolar, An isolated three-port bidirectional DC-DC converter with decoupled power flow management, IEEE Trans. Power Electron. vol. 23 (5) (2008) 2443–2453, https://doi.org/10.1109/tpel.2008.2002056.
[12] O.E. Oyewole and K.H. Ahmed, Comparative Analysis of Decoupling Control Methods for Multiport-isolated Bidirectional Dc-Dc Converter with Hydrogen Storage System Integration, Presented at the 2023 11th International Conference on Smart Grid (icSmartGrid), 2023.
[13] K.O. Bempah, K.-W. Heo, J.-H. Jung, Power flow decoupling method of triple-active-bridge converter for islanding mode operation in DC microgrid systems, J. Power Electron. vol. 23 (1) (2022) 58–67, https://doi.org/10.1007/s43236-022-00528-5.
[14] H. Tao, A. Kotsopoulos, J.L. Duarte, M.A.M. Hendrix, Transformer-coupled multiport ZVS bidirectional DC-DC converter with wide input range, IEEE Trans. Power Electron. vol. 23 (2) (2008) 771–781, https://doi.org/10.1109/TPEL.2007.915129.
[15] D.U. Kim, B. Byen, B. Jeong, and S. Kim, Design of Triple-Active Bridge Converter with Inherently Decoupled Power Flows, in 2022 24th European Conference on Power Electronics and Applications (EPE'22 ECCE Europe), 5-9 Sept. 2022 2022, pp. 1-9.
[16] S. Bandyopadhyay, P. Purgat, Z. Qin, P. Bauer, A multiactive bridge converter with inherently decoupled power flows, IEEE Trans. Power Electron. vol. 36 (2) (2021) 2231–2245, https://doi.org/10.1109/tpel.2020.3006266.
[17] O.M. Hebala, A.A. Aboushady, K.H. Ahmed, I. Abdelsalam, Generalized active power flow controller for multiactive bridge DC-DC converters with minimum-current-point-tracking algorithm, IEEE Trans. Ind. Electron. vol. 69 (4) (2022) 3764–3775, https://doi.org/10.1109/tie.2021.3071681.
[18] K. Zhao, J. Zhang, D. Ma, Y. Xia, Composite disturbance rejection attitude control for quadrotor with unknown disturbance, IEEE Trans. Ind. Electron. vol. 67 (8) (2020) 6894–6903, https://doi.org/10.1109/TIE.2019.2937065.
[19] J. Han, From PID to active disturbance rejection control, IEEE Trans. Ind. Electron. vol. 56 (3) (2009) 900–906, https://doi.org/10.1109/TIE.2008.2011621.
[20] R. Wang, B. Hu, S. Sun, F. Man, Z. Yu, Q. Chen, Linear active disturbance rejection control for DC side voltage of single-phase active power filters, IEEE Access vol. 7 (2019) 73095–73105, https://doi.org/10.1109/ACCESS.2019.2920626.
[21] H. He, T. Si, L. Sun, B. Liu, Z. Li, Linear active disturbance rejection control for three-phase voltage-source PWM rectifier, IEEE Access vol. 8 (2020) 45050–45060, https://doi.org/10.1109/ACCESS.2020.2978579.
[22] S. Zhou, X. Guo, R. Zhang, R. Wang, C. Li, Research on triple interleaved bidirectional DC/DC converter based on second-order linear active disturbance rejection, IEEE J. Emerg. Sel. Top. Power Electron vol. 4 (4) (2023) 1074–1083, https://doi.org/10.1109/JESTIE.2023.3306997.
[23] J. Yang, H. Cui, S. Li, A. Zolotas, Optimized active disturbance rejection control for DC-DC buck converters with uncertainties using a reduced-order GPI observer, IEEE Trans. Circuits Syst. I: Regul. Pap. vol. 65 (2) (2018) 832–841, https://doi.org/10.1109/TCSI.2017.2725386.
[24] K. Łakomy, et al., Active disturbance rejection control design with suppression of sensor noise effects in application to DC-DC buck power converter, IEEE Trans. Ind. Electron. vol. 69 (1) (2022) 816–824, https://doi.org/10.1109/TIE.2021.3055187.
[25] H. Bai, D. Yang, J. Song, Q. Su, B. Duan, C. Zhang, Linear active disturbance rejection control of LLC resonant converters for EV chargers, *2020 Chin. Autom. Congr. (CAC)* (2020) 993–998, https://doi.org/10.1109/CAC51589.2020.9327865.
[26] X. Li, S. Zhan, F. Guo, H. Liao, Z. Zhuang, Linear active disturbance rejection control of dual active bridge converter for portable energy storage system, *2023 5th Int. Conf. Power Energy Technol. (ICPET)* (2023) 35–39, https://doi.org/10.1109/ICPET59380.2023.10367687.
[27] W. Tan, C. Fu, Linear active disturbance-rejection control: analysis and tuning via IMC, IEEE Trans. Ind. Electron. vol. 63 (4) (2016) 2350–2359, https://doi.org/10.1109/TIE.2015.2505668.
[28] T. He, Z. Wu, D. Li, J. Wang, A tuning method of active disturbance rejection control for a class of high-order processes, IEEE Trans. Ind. Electron. (2019), https://doi.org/10.1109/TIE.2019.2908592.
[29] W. Cui, W. Tan, D. Li, Y. Wang, S. Wang, A relay feedback method for the tuning of linear active disturbance rejection controllers, IEEE Access vol. 8 (2020) 4542–4550, https://doi.org/10.1109/ACCESS.2019.2963419.
[30] S. Gong, et al., Sliding mode control-based decoupling scheme for quad-active bridge DC-DC converter, IEEE J. Emerg. Sel. Top. Power Electron. vol. 10 (1) (2022) 1153–1164, https://doi.org/10.1109/jestpe.2021.3096228.
[31] H.-L. Xing, D.-H. Li, J. Li, C.-H. Zhang, Linear extended state observer based sliding mode disturbance decoupling control for nonlinear multivariable systems with uncertainty, Int J. Control Autom. Syst. vol. 14 (4) (2016) 967–976, https://doi.org/10.1007/s12555-014-0420-x.
[32] B.V. Martínez, J. Sanchis, S. García-Nieto, M. Martínez, Active disturbance rejection control: a guide for design and application, Ibero-Am. Mag. Ind. Autom. Inform. vol. 18 (3) (2021) 201–217, https://doi.org/10.4995/riai.2020.14058.

[33] S. Bandyopadhyay, Z. Qin, P. Bauer, Decoupling control of multiactive bridge converters using linear active disturbance rejection, IEEE Trans. Ind. Electron. vol. 68 (11) (2021) 10688–10698, https://doi.org/10.1109/tie.2020.3031531.
[34] Z. Gao, Scaling Parameter Based Controll. Tuning (2003) 4989–4996.
[35] J. Vincent, et al., On active disturbance rejection based control design for superconducting RF cavities, Nucl. Instrum. Methods Phys. Res. Sect. A Accel., Spectrom. Detect. Assoc. Equip. vol. 643 (1) (2011) 11–16, https://doi.org/10.1016/j.nima.2011.04.033.
[36] B. Ferragud and F. Xavier, Predictive Control Based on Models Using Heuristic Optimization Techniques. Application to Nonlinear and Multivariable Processes, Universitat Politècnica de València, Valencia (Spain), 1999. [Online]. Available: ⟨https://riunet.upv.es/handle/10251/15995⟩.
[37] H. Rania, A comparison of particle swarm optimization and the genetic algorithm, in 46th AIAA/ASME/ASCE/AHS/ASC Structure, Structural Dynamics and Materials Conference, Austin, TX, Genetic Algorithm, April 18-21, 2005, 2005.
[38] F.D. Wihartiko, H. Wijayanti, F. Virgantari, Performance comparison of genetic algorithms and particle swarm optimization for model integer programming bus timetabling problem, IOP Conf. Ser. Mater. Sci. Eng. vol. 332 (1) (2018) 012020, https://doi.org/10.1088/1757-899X/332/1/012020.
[39] R. Eberhart, J. Kennedy, A new optimizer using particle swarm theory MHS'95, Proc. Sixth Int. Symp. Micro Mach. Hum. Sci. (1995) 39–43, https://doi.org/10.1109/MHS.1995.494215.